

Three-dimensional tsunami generation simulation due to sea-bottom deformation and its interpretation based on the linear theory

Tatsuhiko Saito^{1,2} and Takashi Furumura^{1,2}

¹Center for Integrated Disaster Information Research, Interfaculty Graduate School of Interdisciplinary Information Studies, the University of Tokyo, Japan.

E-mail: tatsu-saito@bosai.go.jp

²Core Research for Evolutional Science and Technology, Japan Science and Technology Agency, Japan

Accepted 2009 April 3. Received 2009 March 24; in original form 2009 January 22

SUMMARY

The present study investigates the tsunami generation process by using 3-D numerical simulations and the linear potential theory. First, we evaluate the relation between sea-bottom elevation and sea-surface elevation as function of source size L , sea depth H and source duration T , based on 3-D numerical simulations. The surface elevation decreases with increasing sea depth and source duration. The difference between the sea-bottom and the sea-surface elevation appears when the source size is smaller than approximately 10 times the sea depth for a short source duration. The linear potential theory can precisely predict the numerical simulation results. Based on the theory, we can consider the tsunami generation as two spatial lowpass filter processes, in which the cut-off wavenumbers are given by the sea depth and the source duration. The criteria for small source size and short source duration are given as $L < 13H$ and $T < L/(8c)$, respectively, where c is the phase velocity of the tsunami. We then simulate the tsunami generation of the 1896 Sanriku tsunami earthquake, Japan. The simulated sea-surface elevation is significantly different from the sea-bottom elevation, which suggests the need for correction of the sea depth and source duration for the precise evaluation of the initial water-height distribution. To include these effects in 2-D simulations, we can use the impulse response function and add the fractional sea-surface uplift within the time step to the sea surface, for each time step.

Key words: Tsunamis; Computational seismology; Theoretical seismology.

1 INTRODUCTION

The sea-bottom deformation caused by a large earthquake uplifts the sea surface, which acts as a tsunami source. In tsunami simulations based on the 2-D long-wave theory, the initial water-height distribution on the sea surface was often assumed to be identical to the sea-bottom deformation caused by the earthquake (e.g. Ichinose *et al.* 2003). This assumption is widely accepted to be valid when the sea depth is sufficiently shallow compared with the tsunami wavelength and the sea-bottom deformation due to the earthquake occurs within a short period of time. These assumptions in the tsunami excitation can be applied to many tsunamigenic earthquakes occurring in subduction zones, especially for large interplate events, with gently dipping faults. This is, however, not the case for all tsunamigenic earthquakes. For example, outer-ridge events are often characterized by a steep dip angle, which results in the deformation of the sea bottom within a small area, which then results in a small-wavelength tsunami on the sea surface (Saito & Furumura 2009). Another example may be a tsunami earthquake. Tsunami earthquakes are sometimes characterized by very long source durations of more than several dozens of seconds (e.g. Kanamori 1972).

The tsunami generation process has been theoretically investigated, based on the linear approximation method. Analytical solutions can be derived for the spatial and temporal distribution of the tsunami, by solving linear equations for potential water flow with appropriate boundary conditions in a constant sea depth (e.g. Takahashi 1942; Hammack 1973; Kervella *et al.* 2007). We hereinafter refer to the theoretical method as linear potential theory. The linear potential theory indicates that the initial water-height distribution, in general, is not identical to the sea-bottom elevation, but depends strongly on the sea depth and the duration of the sea-bottom deformation. Also, Kajiura (1970) theoretically investigated the effect of the source duration on the tsunami generation from the viewpoint of the energy partition between compressional wave energy and tsunami energy.

Current computers, which are very powerful, enable tsunamis to be simulated in 3-D space without using the approximations used in the long-wave theory and the linear potential theory (Ohmachi *et al.* 2001; Saito & Furumura 2009). The 3-D simulations are suitable for investigating the tsunami generation process because it explicitly calculates the vertical flow of the fluid caused by the sea-bottom elevation. Kakinuma & Akiyama (2006) successfully

simulated through numerical simulations the experimental data obtained by Hammack (1973). 3-D numerical methods have advantages over the linear potential theory. For example, the 3-D simulation can deal with the generation and propagation processes in realistic bathymetry, whereas the linear potential theory is usually limited to the constant sea depth.

The present study investigates the tsunami generation process due to the elevation of the sea bottom, based on both the 3-D tsunami simulation and the linear potential theory. First, we illustrate the tsunami excitation caused by the sea-bottom elevation, with the visualization of water flow calculated by the 3-D numerical simulation. We also conduct tsunami generation simulations for various models of different sea depth, source size and source duration. Then, we interpret the simulation results using the linear potential theory. We show that the tsunami generation can be considered as two spatial low-pass filter processes in which the cut-off wavenumbers are given by the sea depth and the source duration. The criteria for small source size and long source duration are also proposed based on the linear potential theory. Finally, we simulate the tsunami generation using the 1896 Meiji Sanriku tsunami earthquake, as example of an actual earthquake.

2 TSUNAMI GENERATION BY THREE-DIMENSIONAL SIMULATION

2.1 Governing equations for tsunami simulation

The tsunami is a gravity wave, which can be simulated by solving the water motion equations with the boundary conditions at the surface. The incompressible water motion is described by the following 3-D Navier–Stokes equations:

$$\begin{cases} \frac{\partial u}{\partial t} + u \frac{\partial u}{\partial x} + v \frac{\partial u}{\partial y} + w \frac{\partial u}{\partial z} = -\frac{\partial}{\partial x} \left(\frac{p}{\rho_0} \right) + \nu \nabla^2 u, \\ \frac{\partial v}{\partial t} + u \frac{\partial v}{\partial x} + v \frac{\partial v}{\partial y} + w \frac{\partial v}{\partial z} = -\frac{\partial}{\partial y} \left(\frac{p}{\rho_0} \right) + \nu \nabla^2 v, \\ \frac{\partial w}{\partial t} + u \frac{\partial w}{\partial x} + v \frac{\partial w}{\partial y} + w \frac{\partial w}{\partial z} = -\frac{\partial}{\partial z} \left(\frac{p}{\rho_0} \right) + \nu \nabla^2 w - g, \end{cases} \quad (1)$$

in the Cartesian coordinates shown in Fig. 1, where the z -axis is in the vertical direction and the x - and y -axes form a horizontal plane. Velocity components along the x -, y - and z -axes are u , v and w , respectively. The pressure and density of the water are p and ρ , respectively. The parameter ν is the kinematic viscosity coefficient, the value of which is very small ($\nu = 10^{-6} \text{ m}^2 \text{ s}^{-1}$) for sea water. The gravitational acceleration g is 9.8 m s^{-2} .

The continuity equation is given by

$$\frac{\partial u}{\partial x} + \frac{\partial v}{\partial y} + \frac{\partial w}{\partial z} = 0, \quad (2)$$

for incompressible water. A free surface at rest is given as $z = 0$, and the sea bottom is given as $z = -H$, where H is the sea depth. The fluctuation of the sea surface at time t , in the case of a tsunami, is given by $z = \eta(x, y, t)$. The kinematic boundary condition at the sea surface is given by

$$\frac{\partial \eta}{\partial t} + u \frac{\partial \eta}{\partial x} + v \frac{\partial \eta}{\partial y} = w \text{ for } z = \eta(x, y, t). \quad (3)$$

The pressure at the surface is set to be zero, $p(x, y, \eta) = 0$, as a dynamic condition. The above non-linear equations describe the motion of tsunamis.

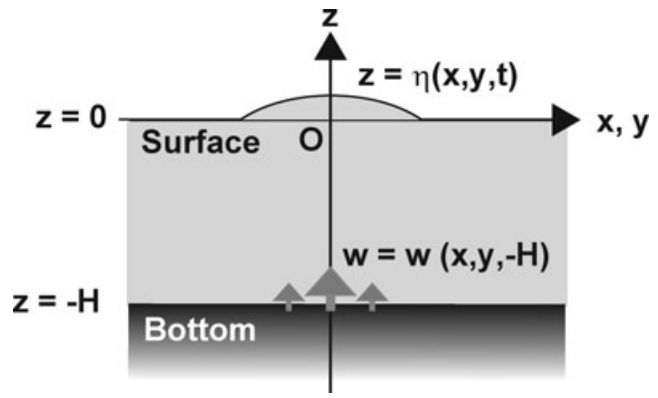


Figure 1. Coordinate system for tsunami equations.

2.2 Tsunami generation simulation

We assume an isotropic distribution of the sea-bottom elevation to obtain a clear perspective for tsunami generation as a function of source size. The final vertical elevation at the sea bottom is assumed to be given by a Gaussian function as

$$d(x, y) = d_0 \exp \left[-\frac{x^2 + y^2}{(L/2)^2} \right]. \quad (4)$$

The distribution is characterized by two parameters, namely, d_0 and L , where d_0 is the maximum height in the deformation at the bottom and L is the source size characterizing the horizontal spatial scale of the deformation area. The elevation of the sea bottom is assumed to occur with a constant elevation speed during the source duration T . The corresponding boundary condition at the sea bottom is included in eq. (1), as the vertical velocity component at the gridpoint of the sea bottom, as follows:

$$w(x, y, -H) = \begin{cases} d(x, y)/T & \text{for } 0 < t \leq T, \\ 0 & \text{for } t > T. \end{cases} \quad (5)$$

Note that when we relate the sea-bottom deformation of eq. (5) with kinematic seismic fault models, eq. (5) includes finite duration of rise time but not rupture propagation; the rupture starts simultaneously on the fault. The vertical flow caused by eq. (5) uplifts the sea surface to produce the initial water-height distribution above the source region.

The three-component velocity and the tsunami height described by eqs (1)–(5) are calculated by the finite-difference method (FDM) based on the technique developed by Hirt *et al.* (1975). The details of the 3-D FDM simulation and the parallel computing procedure are described in Saito & Furumura (2009).

2.3 General view of tsunami generation and propagation

We conduct 3-D FDM simulations of the Navier–Stokes equations to show examples of tsunami generation and propagation caused by sea-bottom deformation. The sea-bottom deformation is characterized by the parameters of $d_0 = 1 \text{ m}$, $L = 40 \text{ km}$ and $T = 60 \text{ s}$ in eqs (4) and (5). The source size of $L = 40 \text{ km}$ roughly corresponds to an $M 7$ earthquake.

Fig. 2 shows cross-sections of the water height at the surface (upper panel) and the water flow distribution from the sea bottom to the sea surface (lower panel) for various elapsed times from the origin time. The tsunami generation process can be classified into

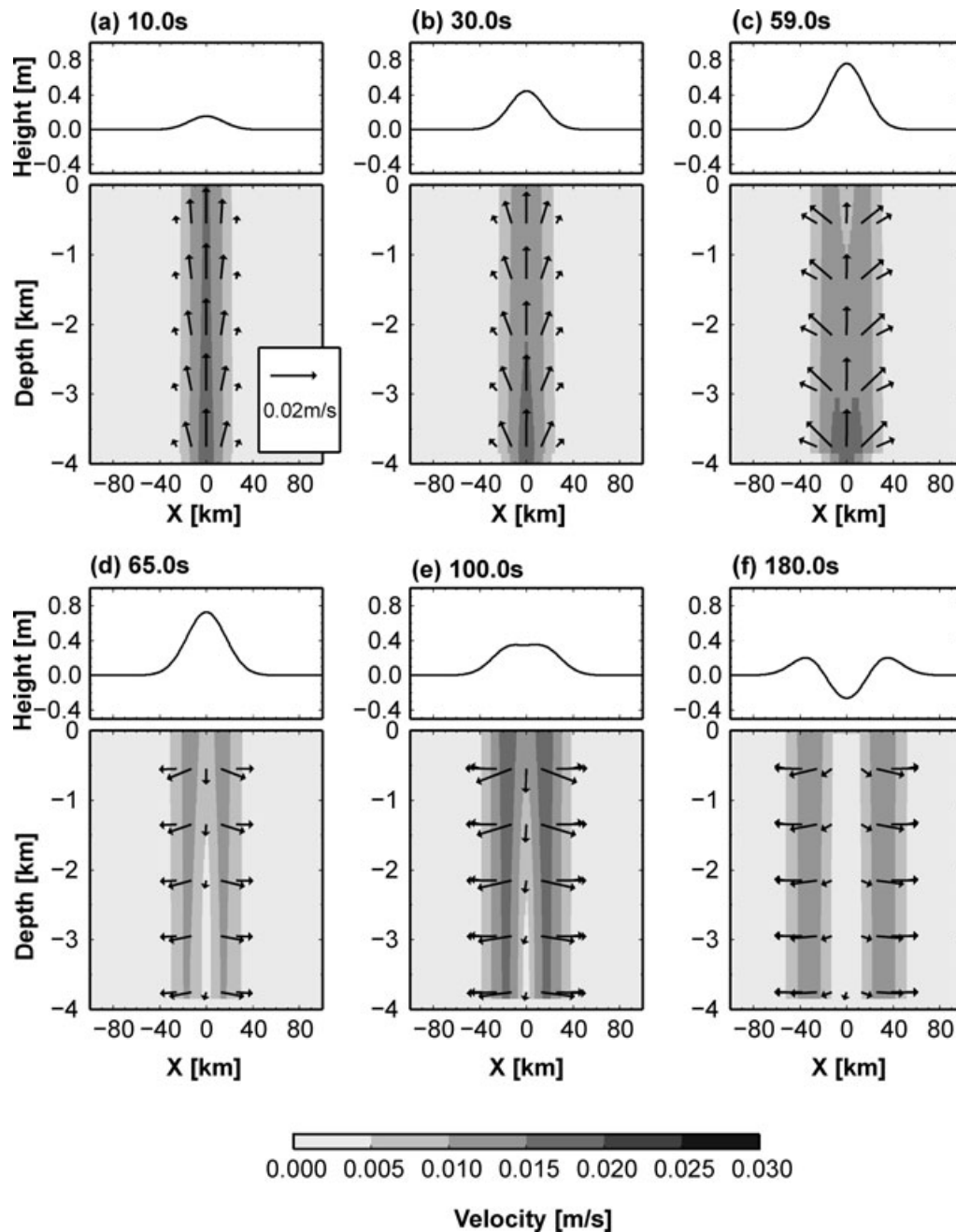


Figure 2. Cross-sections of tsunami generation and propagation for elapsed times of (a) 10, (b) 30, (c) 60, (d) 65, (e) 100 and (f) 180 s from the sea-bottom-deformation starting time. The surface height distribution along the x -axis is plotted in the upper panels, and the velocity distribution is shown in the lower panels for each elapsed time. The results are calculated with 3-D numerical tsunami simulation for sea-bottom deformation characterized by $d_0 = 1$ m, $L = 40$ km and $T = 60$ s.

three stages. At the time before the source process time ($T < 60$ s), the sea-bottom elevation produces vertical flow of water over the source region (Figs 2a–c). As time passes, the horizontal velocity increases, as the tsunami propagates away from the source region. In the second stage, as the source rupture ends ($T = 60$ s), and the vertical velocity provided by the sea bottom disappears. The collapse of the uplifted surface accelerates (Fig. 2d), which causes descending flow. In the third stage (Figs 2e and f), or in the time during which the tsunami propagates away from the source region, the horizontal velocities becomes dominant over the vertical velocity throughout the depth range. The distribution of horizontal velocity

is almost invariant in depth (Fig. 2f). Such a velocity distribution pattern is assumed in the tsunami propagation model, based on the long-wave theory (e.g. Stoker 1958).

2.4 Tsunami generation variation with various model parameters

We conduct 3-D tsunami simulations to obtain quantitative relations between the water-height distribution at the surface and the sea-bottom elevation. Fig. 3 compares the water-height

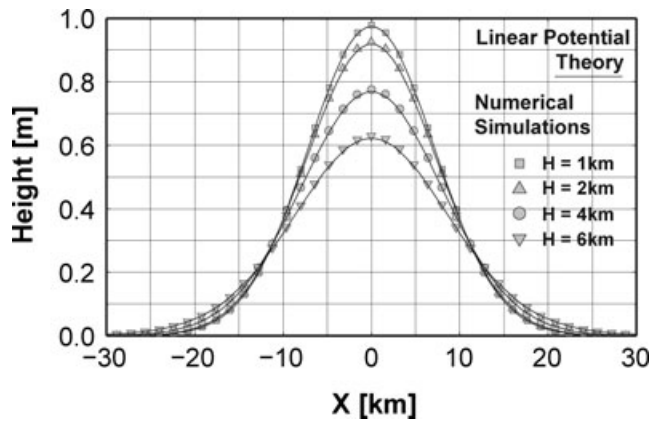


Figure 3. Initial water-height distribution for various sea depths— $H = 1, 2, 4$ and 6 km. The sea-bottom deformation is given by the Gaussian function of $d_0 = 1$ m, $L = 20$ km and $T = 10$ s in eqs (4) and (5). Numerical simulation results are plotted by symbols, and the values obtained from the linear potential theory are plotted by the solid curve.

distributions for a common source of $d_0 = 1$ m, $L = 40$ km and $T = 10$ s with respect to various sea depths of $H = 1, 2, 4$ and 6 km. The cross-sections calculated by the simulations with different sea depths are plotted by different symbols. The water-height distribution is measured at the time when the sea-bottom deformation ends. We hereinafter refer to the water-height distribution as the initial water-height distribution. The maximum height in the initial water-height distribution decreases, and the width of the distribution increases with increasing sea depth. The maximum water-height for a shallow sea ($H = 1$ km, plotted by squares in Fig. 3) is 0.97 m, which is approximately the same as that of the sea-bottom elevation ($d_0 = 1$ m). However, the maximum water-height for a deep sea ($H = 6$ km, plotted by inverted triangles in Fig. 3) is significantly smaller (0.62 m) than that of the sea-bottom elevation and has a relatively wider distribution.

Fig. 4 shows cross-sections of the initial water-height distribution for a common source of $d_0 = 1$ m and $T = 10$ s with respect to various source sizes, $L = 80, 40$ and 20 km. The depth H is set to be 4 km throughout this simulation. The water height at the sea surface decreases with decreasing source size L . For the result of the wide source model ($L = 80$ km; plotted by squares in Fig. 4), the

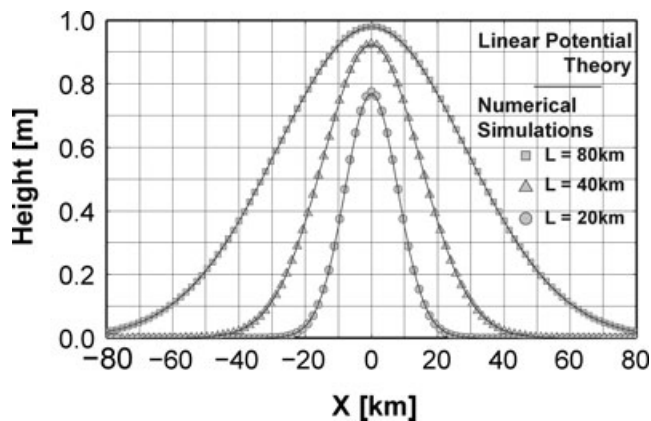


Figure 4. Initial water-height distribution for various source size, $L = 80, 40$ and 20 km, at the sea depth of $H = 4$ km. The sea-bottom deformation is given by the Gaussian function of $d_0 = 1$ m and $T = 10$ s in eqs (4) and (5). Numerical simulation results are plotted by symbols, and the values obtained from the linear potential theory are plotted by the solid curve.

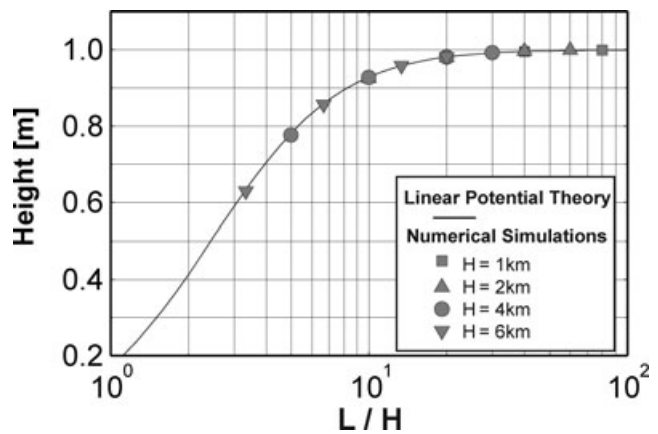


Figure 5. Maximum height at the surface with respect to source size L normalized by the sea depth H for a source duration T of 10 s. Numerical simulation results are plotted by symbols, and the values obtained from the linear potential theory are plotted by the solid curve.

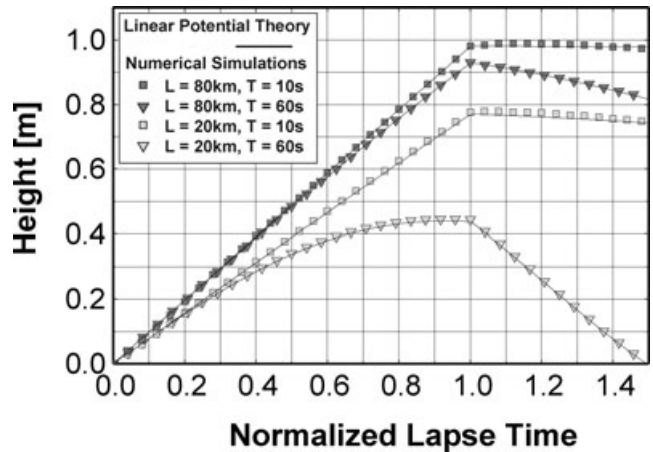


Figure 6. Water-height variation with respect to the elapsed time normalized by the source duration T . The height is measured at the centre of the source region ($x = 0, y = 0$). Numerical simulation results are plotted by symbols, and the values obtained from the linear potential theory are plotted by the solid curve.

maximum water height (0.98 m) is almost as high as the sea-bottom elevation. However, the maximum water height for the small source model ($L = 20$ km) is less than approximately 80 per cent (0.77 m) of the sea-bottom elevation.

We then conduct a set of tsunami generation simulations for $T = 10$ s, using various source sizes of $L = 20, 40, 80$ and 120 km and sea depths of $H = 1, 2, 4$ and 6 km. We obtain a simple relation for the maximum height of the initial water-height distribution as a function of source size relative to the sea depth (L/H ; symbols in Fig. 5). All plots of the simulated water-height for different source sizes and sea depths follow a simple curve, and the maximum height increases with increasing normalized source size L/H . This relation indicates that when the source size L is larger than approximately 10 times the sea depth, the initial water-height distribution is almost identical to the sea-bottom deformation.

Then, we investigate the effect of the source duration on the initial water-height distribution. Fig. 6 shows the water height at the centre ($x = 0$ and $y = 0$) as a function of time t , normalized by the source duration (t/T). The water height increases linearly with increasing time and takes its maximum value at time $t = T$. After

the sea-bottom elevation ends ($t > T$), the water height gradually decreases with increasing time. For the large source ($L = 80$ km), the initial water-height distributions are approximately identical to the sea-bottom elevation distribution. However, a small source ($L = 20$ km) cannot uplift the water height efficiently. Slowly uplifting the sea bottom, which is characterized by a long source duration ($T = 60$ s), does not produce an initial water-height distribution as high as that produced by a quickly uplifting sea bottom, which is characterized by a short source duration ($T = 10$ s). In the case of a small source size ($L = 20$ km), the maximum amplitudes of the tsunami are 0.44 and 0.77 m for the source durations of $T = 60$ and 10 s, respectively, which is much smaller than the sea-bottom elevation ($d_0 = 1$ m).

3 LINEAR POTENTIAL THEORY FOR TSUNAMI GENERATION

To interpret the tsunami generation process and the simulation results obtained in the previous section, we employ the linear potential theory. Assuming small amplitude and irrotational flow, this theory uses velocity potential and approximates the non-linear equations to linear equations (e.g. Takahashi 1942; Ward 2001; Kervella *et al.* 2007).

3.1 Linear potential theory

We assume that the final sea-bottom deformation is given by $d(x, y)$ and that the corresponding boundary condition for the vertical velocity at the bottom is given by

$$w_B(x, y, -H) = d(x, y) \chi(t), \quad (6)$$

where the function $\chi(t)$ depends only on time and satisfies the following:

$$\int_{-\infty}^{\infty} \chi(t) dt = 1, \quad (7)$$

and has the dimension of the inverse of time. Using eq. (6) as the bottom boundary condition in the linear potential theory, the sea-surface $\eta(x, y, t)$ is given by

$$\eta(\mathbf{x}, t) = \frac{1}{(2\pi)^2} \int_{-\infty}^{\infty} \int_{-\infty}^{\infty} d\mathbf{k} \exp(i\mathbf{k} \cdot \mathbf{x}) \times \int_{-\infty}^t d\tau \chi(\tau) \cos \gamma(t - \tau) \frac{1}{\cosh kH} \hat{d}(\mathbf{k}), \quad (8)$$

where \mathbf{k} is the wavenumber vector given by $\mathbf{k} = k_x \mathbf{e}_x + k_y \mathbf{e}_y$ and $k = \sqrt{k_x^2 + k_y^2}$ and the parameter γ is given by

$$\gamma \equiv k \sqrt{gH} \sqrt{\frac{1}{kH} \tanh kH}. \quad (9)$$

The $\hat{d}(\mathbf{k})$ in eq. (8) is the 2-D spatial Fourier transformation given by

$$\hat{d}(\mathbf{k}) = \int_{-\infty}^{\infty} \int_{-\infty}^{\infty} dx dy d(x, y) \exp(-i\mathbf{k} \cdot \mathbf{x}). \quad (10)$$

Eq. (8) was originally derived by Takahashi (1942) in cylindrical coordinates and was also obtained by Kervella *et al.* (2007) using a complex integral range with respect to time (Laplace transform). The present study uses the Cartesian coordinates and real integral range of time (Fourier transform) in eq. (8). An outline of the derivation of the linear potential theory is provided in Appendix A.

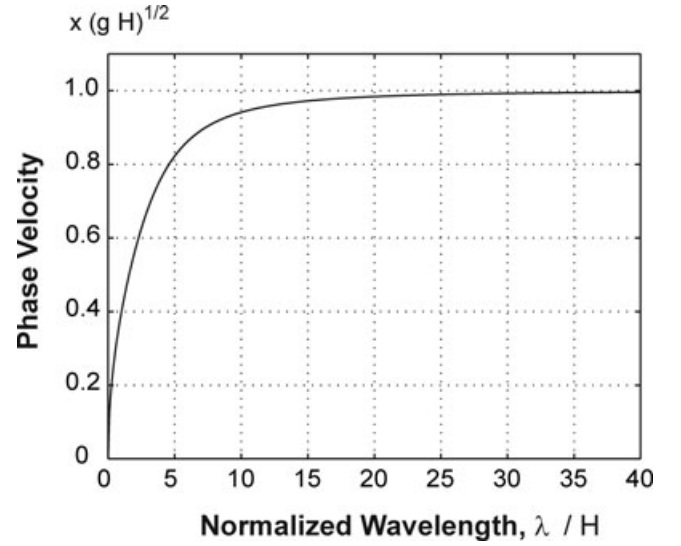


Figure 7. Phase velocity with respect to the wavelength λ normalized by the sea depth H .

When the velocity of the sea-bottom uplifting is constant (eq. 5), eq. (8) is simplified as

$$\eta(\mathbf{x}, t) = \begin{cases} \frac{\xi(\mathbf{x}, t)}{T} & \text{for } 0 < t < T \\ \frac{\xi(\mathbf{x}, t) - \xi(\mathbf{x}, t - T)}{T} & \text{for } t \geq T \end{cases}, \quad (11)$$

where the function $\xi(\mathbf{x}, t)$ is given by

$$\xi(\mathbf{x}, t) = \frac{1}{(2\pi)^2} \int_{-\infty}^{\infty} \int_{-\infty}^{\infty} d\mathbf{k} \exp(i\mathbf{k} \cdot \mathbf{x}) \frac{\sin \gamma t}{\gamma} \frac{1}{\cosh kH} \hat{d}(\mathbf{k}). \quad (12)$$

Since eq. (8) indicates that the sea surface η can be considered as the sum of the 2-D plane waves of the wavenumber k , and the parameter γ is the angular frequency, the phase velocity of the tsunami as a function of the wavenumber is given by

$$c(k) = \frac{\gamma}{k} = c_0 \sqrt{\frac{1}{kH} \tanh kH} \approx c_0 \left\{ 1 - \frac{1}{6} (kH)^2 \right\} \text{ when } kH \ll 1, \quad (13)$$

where $c_0 \equiv \sqrt{gH}$ is the phase velocity of the tsunami obtained by the linear long-wave theory, in which the tsunami wavelength is assumed to be much longer than the sea depth (e.g. Stoker 1958). The phase velocity c is plotted in Fig. 7 as a function of the tsunami wavelength. The phase velocity increases gradually with increasing wavelength and approaches the value of c_0 .

3.2 Comparisons with 3-D numerical simulations

From eqs (11) and (12) with the Gaussian-function source (4), we calculate the spatial temporal variation of the sea-surface fluctuation for comparison with the numerical simulation results in Figs 3–6. The solutions based on eqs (11) and (12) are plotted by solid curves, and the numerical simulation results are plotted by symbols. All of the figures show excellent agreement between the solutions of the linear potential theory and the 3-D numerical simulations. This agreement is reasonable because the linear approximation is assumed to be valid when the tsunami height (~ 1 m) is much smaller than the sea depth (~ 1000 m).

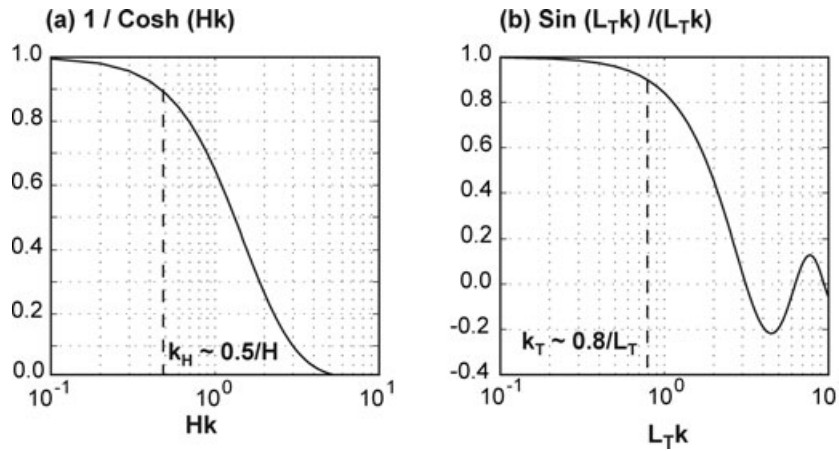


Figure 8. Functions (a) $1/\cosh(Hk)$ and (b) $\sin(L_T k)/(L_T k)$.

3.3 Tsunami generation as a filtering process

We interpret the tsunami generation process based on the linear potential theory. Substituting t for T in eqs (11) and (12), we obtain the relation between the initial water-height distribution and the sea-bottom deformation as follows:

$$\begin{aligned} \eta(\mathbf{x}, T) &= \frac{\xi(\mathbf{x}, T)}{T} = \frac{1}{(2\pi)^2} \int_{-\infty}^{\infty} \int_{-\infty}^{\infty} d\mathbf{k} \\ &\quad \times \exp(i\mathbf{k} \cdot \mathbf{x}) \frac{1}{\cosh kH} \frac{\sin \gamma T}{\gamma T} \hat{d}(\mathbf{k}) \\ &= F^{-1} \left[\frac{1}{\cosh kH} \frac{\sin \gamma T}{\gamma T} \hat{d}(\mathbf{k}) \right] \\ &= F^{-1} \left[\frac{1}{\cosh kH} \frac{\sin L_T k}{L_T k} \hat{d}(\mathbf{k}) \right], \end{aligned} \tag{14}$$

where $F^{-1}[\dots]$ is the 2-D inverse Fourier transform with respect to wavenumber k . In addition, L_T is a characteristic distance given by $L_T = cT$, where c is the phase velocity given by eq. (13). The distance L_T is the tsunami propagation distance during the source duration T .

The factor $(1/\cosh kH) \sin L_T k/L_T k$ is considered to be a short-wavelength cut filter for the distribution of sea-bottom elevation $\hat{d}(\mathbf{k})$, which leads to a smooth initial water-height distribution $\eta(\mathbf{x}, T)$. The factor $(1/\cosh kH) \sin L_T k/L_T k$ can be decomposed into two parts: the former is related to the sea depth H as $1/\cosh Hk$, and the latter is related to the source duration T as $\sin \gamma T/\gamma T$.

Fig. 8(a) shows a short-wavelength cut filter $1/\cosh Hk$ as a function of Hk . This filter is characterized by a corner wavenumber $k_H = 0.5/H$, when we define the corner wavenumber as $1/\cosh Hk_H = 0.9$. This filter eliminates the small-scale variation in the initial water-height distribution, in which the wavenumber is larger than the corner wavenumber k_H . Roughly speaking, small-scale spatial variation of the sea-bottom deformation having a wavelength smaller than $13H$ ($= 2\pi/k_H$) disappears in the initial water-height distribution due to this filtering effect. This has been shown by the 3-D simulation results (Figs 3 and 5). We hereinafter refer to the filter $1/\cosh Hk$ as the depth filter.

Fig. 8(b) shows a short-wavelength cut filter $\sin L_T k/L_T k$ as a function of $L_T k$. This filter is characterized by a corner wavenumber of $k_T = 0.8/L_T$, where L_T is a characteristic length given by the source duration T as $L_T = cT$. The filter eliminates the small-scale variation of the sea-bottom deformation having a wavenumber larger than the corner wavenumber k_T . Roughly speaking, small-scale spatial variation of the sea-bottom deformation having a wave-

length smaller than $8L_T$ ($= 2\pi/k_T$) disappears in the initial water-height distribution due to this filtering effect. We hereinafter refer to this filter as the duration filter.

3.4 Three corner wavenumbers in the tsunami generation process

In addition to the above two corner wavenumbers, k_H and k_T , we introduce a corner wavenumber K_S for the spectral contents of the sea-bottom deformation. Using these three corner wavenumbers, we classify the tsunamigenic earthquakes with respect to sea depth H , source size L and source duration T (Table 1).

In the first type [(a) in Table 1] of tsunamigenic earthquake, the sea-bottom deformation is characterized by the area being much larger than the sea depth, $L \gg 13H$, and a small source duration, $T \ll L/(8c)$. In this case, the relation among the depth filter, the duration filter and the spectral contents of the sea-bottom deformation is schematically illustrated in Fig. 9(a). In this case, since neither the depth nor the duration filters affect the spectral contents of the sea-bottom deformation, the resultant initial water-height distribution is approximately identical to the sea-bottom deformation distribution. For example, large and shallowly dipping interplate events that uplift large areas at the sea bottom are classified as this type of tsunamigenic earthquake.

In the second type [(b) in Table 1] of tsunamigenic earthquake, the sea-bottom deformation is characterized by a small area $L < 13H$ or the sea-bottom deformation contains significant large-wavenumber components. In this case, the depth filter plays an important role to remove large-wavenumber components of the sea-bottom deformation during the tsunami generation process (Fig. 9b). For example, events with a large dip angle are classified as this type of tsunamigenic earthquake because they produce sea-bottom deformation in a small area. Events that occurred at very shallow depth are also classified into this type of tsunamigenic earthquake because these events cause steep sea-bottom deformations that are composed of large-wavenumber components.

The third type [(c) in Table 1] of tsunamigenic earthquake is characterized by the long source duration $T > L/(8c)$. In this case, the duration filter should be taken into account in the tsunami generation process (Fig. 9c). For example, tsunami earthquakes, which are sometimes characterized by long source duration, may be classified into this type of tsunamigenic earthquake.

Table 1. Classification of the tsunami source.

| Source type | Criteria of wavenumber domain | Criteria of space and time domain | Corrections for initial water-height distribution | Examples of event type |
|---|-------------------------------|-----------------------------------|---|---|
| (a) Large source area, short process-time | $K_S \ll k_H, k_T$ | $L \gg 13H$ $T \ll L/(8c)$ | No need | Large, interplate events |
| (b) Small source area | $K_S > k_H$ | $L < 13H$ | Sea depth correction (e.g. Kajiura's equation) | Intraplate events, shallow-depth events |
| (c) Long source process time | $K_S > k_T$ | $T > L/(8c)$ | Source duration correction | Tsunami earthquakes |

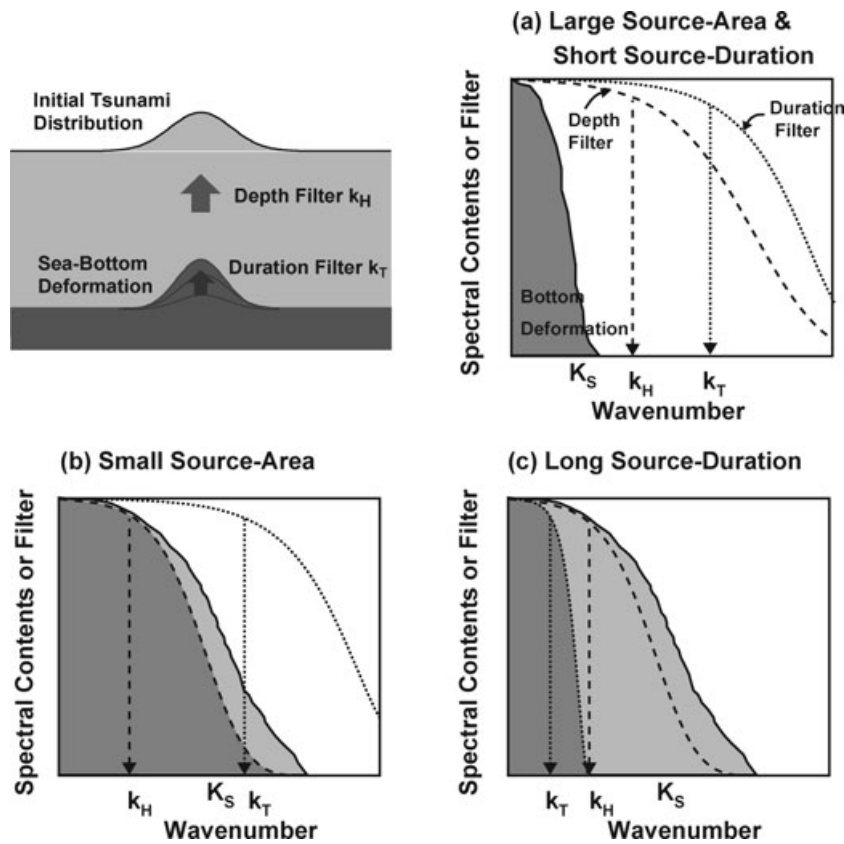


Figure 9. Schematic diagrams for filtering effect in the tsunami generation process for various cases: (a) large source area and short source duration; (b) small source area and (c) long source duration. The spectral contents of the sea-bottom deformation are indicated by the shaded area with the corner wavenumber K_S . The filter associated with the sea depth is indicated by the coarse dashed curve with the corner wavenumber k_H . The filter associated with the source duration is indicated by the fine dashed curve with the corner wavenumber k_T . The spectral contents removed by the filters are indicated by the light grey area.

4 SIMULATION OF THE INITIAL WATER-HEIGHT DISTRIBUTION FOR THE 1896 SANRIKU TSUNAMI EARTHQUAKE

This section considers the depth and source duration effects on the initial water-height distribution by simulating the 1896 Sanriku tsunami earthquake as an example of an actual event. The 1896 Sanriku tsunami earthquake was an interplate event occurring between the North American and the Pacific plates (Fig. 10) and was considered to be a tsunami earthquake, which is characterized by a large tsunami magnitude ($M_t = 8.6$) and a small surface-wave magnitude ($M_s = 7.2$; e.g. Abe 1979). The fault parameter was estimated by Tanioka & Satake (1996) and Tanioka & Seno (2001) from the tsunami records. The fault geometry is characterized by

a gently dipping fault plane of approximately 10° – 20° and the top depth of the fault plane is estimated as 0 km in their studies.

4.1 Three-dimensional tsunami generation simulations

Fig. 11(a) shows the sea-bottom deformation calculated from the fault parameters of Tanioka & Satake (1996). The deformation is calculated by using the solution of Okada (1985), assuming a half-space homogeneous medium. The fault area is 210 km in length and 50 km in width. The dip angle is 20° , and the rake angle is 90° . The slip on the fault is 5.7 m. The slip in the shallow part of the fault causes the sharp deformation at the sea bottom. The maximum elevation of the sea bottom is 2.8 m. The corresponding

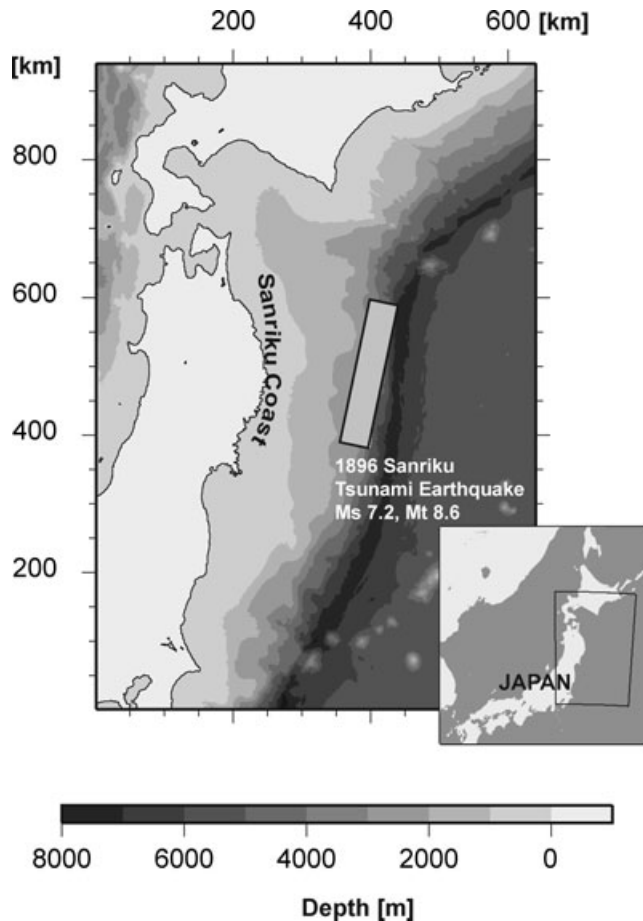


Figure 10. Bathymetry around the source region of the 1896 Sanriku tsunami earthquake. The large rectangle shows the fault location.

spectral amplitude in the x -component is also plotted in the right-hand panel.

Using the sea-bottom elevation distribution in the boundary condition of eq. (5), we calculate the initial water-height distribution by the 3-D N-S simulation to show the effects of the sea depth and the source duration on the tsunami generation. Since the source duration of the 1896 Sanriku earthquake was unknown, we examine the two cases—for short ($T = 10$ s) and long ($T = 100$ s) source durations. A short source duration ($T = 10$ s) is typical for usual earthquakes. On the other hand, the long source process time of $T = 100$ s was reported in the 1992 Nicaraguan earthquake, as a tsunami earthquake (Ide *et al.* 1993; Imamura *et al.* 1993). The critical source process time $L/8c$ introduced in the previous section is approximately 30 s for this event. The left-hand panels in Figs 11(b) and (c) show the simulated initial water-height distribution for short and long source duration models, respectively. For the case of short source duration ($T = 10$ s), the maximum height of the initial water-height is approximately 1.8 m, which is 66 per cent of the sea-bottom elevation (2.7 m; Fig. 11(b)). This case is classified as type (b) in Table 1. The corresponding spectral amplitude of the initial water-height distribution (black solid line) is plotted in the right-hand panel, together with the depth (coarse dashed line) and source duration (fine dashed line) filters. The depth filter eliminates wavenumber components larger than approximately 0.1 km^{-1} from the sea-bottom deformation, whereas the duration filter does not affect the sea-bottom deformation. The case of the long source duration ($T = 100$ s) classified as type (c) in Table 1 is shown in

Fig. 11(c). The maximum tsunami height in this case is 1.4 m, which is 54 per cent of the sea-bottom elevation and 81 per cent of that for the case of short source duration ($T = 10$ s). The duration filter eliminates wavenumber components larger than approximately 0.05 km^{-1} from the sea-bottom deformation. The above two simulation results (Figs 11b and c) indicate that the sea depth and the variation of the source duration can significantly affect the initial water-height distribution in this event.

4.2 Conventional correction method in 2-D simulation for implementing depth and duration effects

A correction method was employed in conventional 2-D tsunami simulations for including the depth and duration effects in the tsunami generation process. The effects of the sea depth can be taken into account by an impulse response function,

$$G(x, y) = \frac{1}{2\pi} \int_0^\infty dk J_0(k\sqrt{x^2 + y^2}) k \frac{1}{\cosh kH}, \quad (15)$$

with respect to a point source of vertical velocity at the bottom (Appendix B). This equation is the same as eq. (39) in Kajiura (1963), and it is hereinafter referred to as Kajiura's equation. To include the source duration effect, the sea-bottom elevation within the time step is added to the sea surface, for each time step (e.g. Fujii & Satake 2008). Although some studies took into account both of these effects in the evaluation of the initial water-height distribution in 2-D tsunami simulations (e.g. Tanioka & Seno 2001), many studies have neglected one or the other of these effects. Figs 12(b) and (e) show the water-height distribution evaluated by the conventional method using eq. (15) and taking the source process times of 10 and 100 s into account by the same method as Fujii & Satake (2008). These simulation results show excellent agreement with the 3-D N-S simulation results (Figs 12a and d). The agreement indicates that the conventional correction method used in the 2-D tsunami simulation can be used to properly evaluate the initial water-height distribution. On the other hand, the water height distributions calculated based on the linear potential theory given by eq. (14) (Figs 12c and f) are slightly different from the 3-D N-S simulation results. The difference is mainly due to the assumption of the constant sea depth ($H = 4 \text{ km}$) in eq. (14). Although the difference would be very small compared with those caused by other uncertainties, such as seismic fault and subsurface structure models, the conventional method using eq. (15) and including source duration effect (e.g. Fujii & Satake 2008) are more appropriate in evaluating initial water-height distribution than the direct use of eq. (14).

5 DISCUSSION AND CONCLUSIONS

We evaluated the relation between the sea-bottom elevation and the sea-surface elevation as a function of the source size L , sea depth H and duration T , based on the 3-D tsunami simulation. When the source size L is much larger than the sea depth H , the initial water-height distribution is approximately the same as the bottom deformation. This situation is often assumed in conventional studies. However, the water height, in general, decreases with increasing sea depth H and the duration T (Figs 3, 4, 5 and 6). When the duration is short enough, the difference between the initial water-height distribution and the sea-bottom deformation appears when the source size is smaller than approximately 10 times the sea depth (Fig. 5).

The linear potential theory can predict the above simulation results quantitatively. Furthermore, based on the linear potential

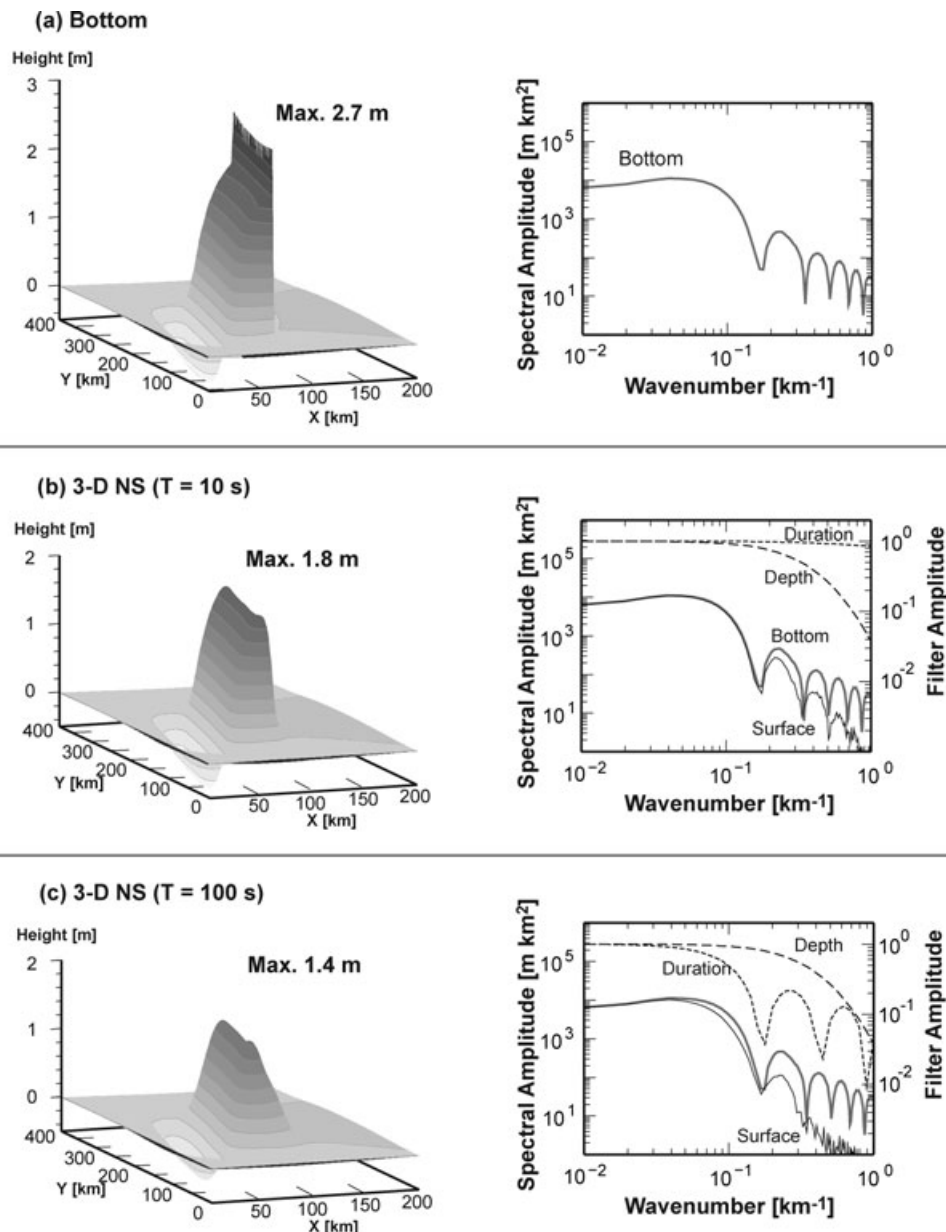


Figure 11. (a) Sea-bottom deformation and initial water-height distribution for the source process times of (b) 10 s and (c) 100 s in the 1896 Sanriku tsunami earthquake. The left-hand panels in (b) and (c) are the initial water-height distribution calculated with 3-D numerical simulations. The right-hand panels in (b) and (c) show the spectral amplitude in the x -component (black solid curve), estimated from the simulation results together with the spectral amplitude of the sea-bottom deformation (grey bold curve). The amplitude of the depth and duration filters are plotted by coarse and fine dashed curves, respectively.

theory, tsunami generation process can be considered as a filtering process in the wavenumber domain. The spatial spectrum of the initial water-height distribution is obtained by applying the two low-pass filters on the spatial spectrum of the sea-bottom deformation. A corner wavenumber is given by $0.5H^{-1}$, and the other wavenumbers are given by $0.8c^{-1}T^{-1}$, in terms of the phase velocity c and the duration T . This indicates that the effect of the sea depth should be taken into account when the source size L is smaller than $13H$, and the source duration T , when the source duration is longer than $L/(8c)$ in the tsunami generation.

The tsunami generation process of the 1896 Sanriku tsunami earthquake is simulated as an example of actual event. The initial water-height distribution is significantly different from the sea-bottom deformation; the maximum height of the surface is ap-

proximately 66 per cent of the maximum height at the bottom. In addition, the initial water-height distribution depends significantly on the source duration. It is necessary to include the effects of both the sea depth and the source duration for precise reproduction of the initial water-height distribution from the sea-bottom deformation in the 1896 Sanriku event. From the comparisons between the 3-D and 2-D tsunami generation simulations, we confirmed that to implement the depth and duration effects in 2-D tsunami simulation, we can use the impulse response function (eq. (15)) to include the effect of the sea depth and add the fractional sea-surface uplift within the time step to the sea-surface, for each time step, to include the finite source duration.

This study has investigated the effects of the source duration on the tsunami generation, assuming that the sea-bottom deformation

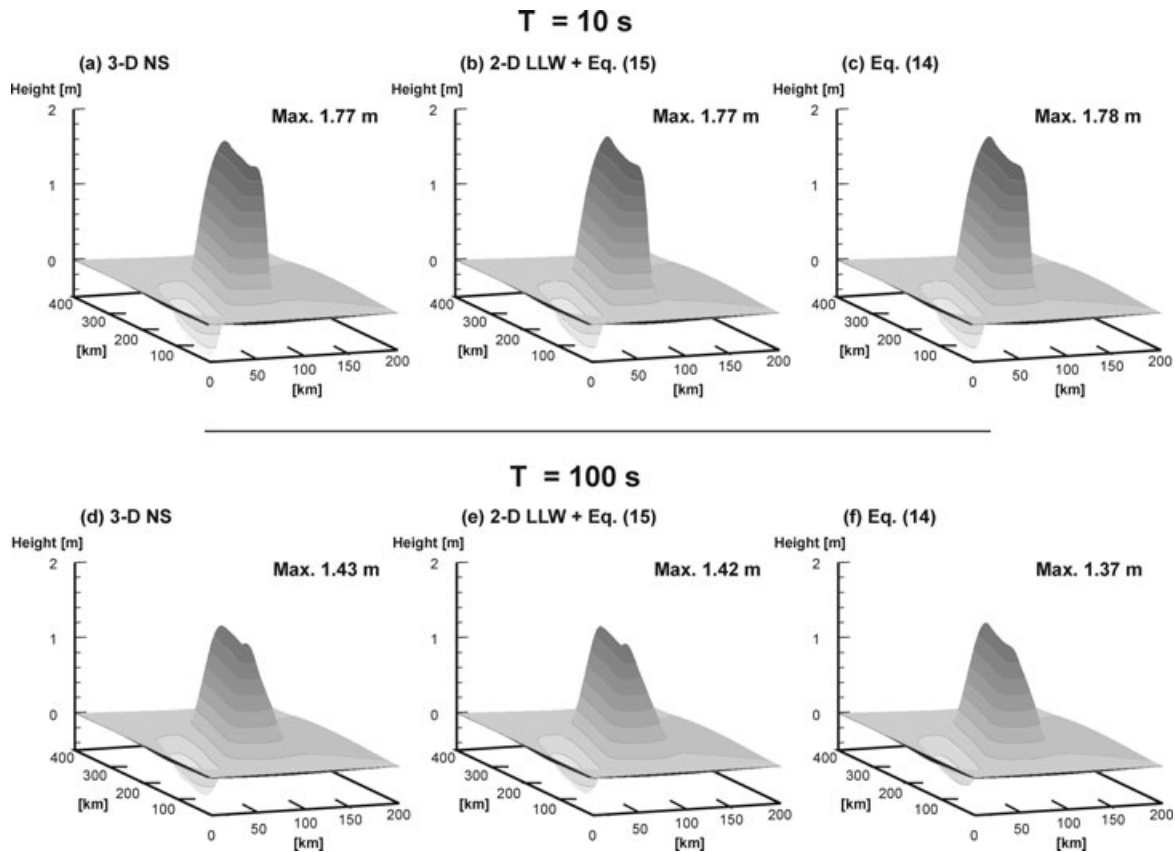


Figure 12. Initial water-height distribution for the source duration T of 10 s (a–c) and 100 s (d–f). (a) and (d) are numerically simulated by 3-D Navier–Stokes equations; (b) and (e) are numerically simulated by 2-D linear long-wave (LLW) equations with eq. (15); and (c) and (f) are calculated based on eq. (14).

is characterized by eq. (5). We may consider that the sea-bottom deformation is caused by a seismic fault with finite rise time T but does not include the rupture propagation. Some studies investigate the tsunami generation considering the finite rupture velocity, based on the linear potential theory (e.g. Ben-Menahem & Rosenman 1972; Ward 2001). Because those studies use some approximations to obtain analytical solutions, it would be important to examine the validity based on the 3-D simulations. Furthermore, it would also be important to study the tsunami generation process in real bathymetry, including both finite rise time and rupture velocity.

The comparisons of 3-D and 2-D simulation results in this study confirm the validity of the conventional technique in 2-D simulations. Since 2-D simulation is much more efficient than 3-D simulation with respect to computational cost, at present, it would be better to use the 2-D method in practice. However, steadily increasing computer power and parallel computing techniques using a large number of processors will enable us to conduct large-scale 3-D simulations in far less computational time. In addition, the 3-D simulation naturally simulates all of the wave phenomena in not only the generation process but also the propagation process. For example, wave dispersion, which is not simulated by the linear long-wave equations, would occur in the tsunamis propagation (Saito & Furumura 2009). Hence, it would also be important to develop efficient tsunami computation methods in 3-D.

ACKNOWLEDGMENT

This study was supported by a grant-in-aid from the Core Research for Evolutional Science and Technology (CREST), the Japan Sci-

ence and Technology Agency. We thank to the Earth Simulator Center, Japan Marine-Earth Science and Technology (JAMSTEC) and Earthquake Information Center, Earthquake Research Institute, for supporting CPU time. Careful reading of the manuscript and constructive comments by K. Satake, M. Korn and anonymous reviewers were very valuable for revision.

REFERENCES

- Abe, K., 1979. Size of great earthquakes of 1837–1974 inferred from tsunami data, *J. Geophys. Res.*, **84**, 1561–1568.
- Ben-Menahem, A. & Rosenman, M., 1972. Amplitude patterns of tsunami waves from submarine earthquakes, *J. Geophys. Res.*, **77**, 3097–3128.
- Fujii, Y. & Satake, K., 2008. Tsunami sources of the November 2006 and January 2007 great Kuril earthquakes, *Bull. Seism. Soc. Am.*, **98**, 1559–1571, doi:10.1785/0120070221.
- Hammack, J.L., 1973. A note on tsunamis: their generation and propagation in an ocean of uniform depth, *J. Fluid Mech.*, **60**, 769–799.
- Hirt, C.W., Nichols, B.D. & Romero, N.C., 1975. SOLA—A numerical solution algorithm for transient fluid flows, Los Alamos National Laboratory report, LA-5852.
- Ichinose, G.A., Thio, H.K. & Somerville, P.G., 2003. Rupture process of the 1944 Tonankai earthquake (M_S 8.1) from the inversion of teleseismic and regional seismograms, *J. geophys. Res.*, **108**, B10,2497, doi:10.1029/10.1029/2003JB002393.
- Ide, S., Imamura, F., Yoshida, Y. & Abe, K., 1993. Source characteristics of the Nicaraguan tsunami earthquake of September 2, 1992, *Geophys. Res. Lett.*, **20**, 863–866.
- Imamura, F., Shuto, N., Ide, S., Yoshida, Y. & Abe, K., 1993. Estimate of the tsunami source of the 1992 Nicaraguan earthquake from tsunami data, *Geophys. Res. Lett.*, **20**, 1515–1518.

- Kajiura, K., 1963. The leading wave of a tsunami, *Bull. Earthq. Res. Ins.*, **41**, 545–571.
- Kajiura, K., 1970. Tsunami source, energy and the directivity of wave radiation, *Bull. Earthq. Res. Ins.*, **48**, 835–869.
- Kakinuma, T. & Akiyama, M., 2006. Numerical analysis of tsunami generation due to seabed deformation (in Japanese with English abstract), *Doboku Gakkai Ronbunshuu B*, **62**, 388–405.
- Kanamori, H., 1972. Mechanism of tsunami earthquake, *Phys. Earth planet. Inter.*, **6**, 246–259.
- Kervella, Y., Dutykh, D. & Dias, F., 2007. Comparison between three-dimensional linear and nonlinear tsunami generation models, *Theor. Comput. Fluid Dyn.*, **21**, 245–269.
- Ohmachi, T., Tsukiyama, H. & Matsumoto, H., 2001. Simulation of tsunami induced by dynamic displacement of seabed due to seismic faulting, *Bull. seism. Soc. Am.*, **91**, 1898–1909.
- Okada, Y., 1985. Surface deformation due to shear and tensile faults in a half space, *Bull. seism. Soc. Am.*, **75**, 1135–1154.
- Saito, T. & Furumura, T., 2009. Three-dimensional simulation of tsunami generation and propagation: application to Intraplate events, *J. geophys. Res.*, **114**, B02307, doi:10.1029/2007JB005523.
- Stoker, J.J., 1958. *Water Waves: The Mathematical Theory with Applications*, John Wiley and Sons, Inc., New York.
- Takahashi, R., 1942. On seismic sea waves caused by deformations of the sea bottom (in Japanese with English abstract), *Bull. Earthq. Res. Inst.*, **20**, 357–400.
- Tanioka, Y. & Satake, K., 1996. Fault parameters of the 1896 Sanriku tsunami earthquake estimated from tsunami numerical modeling, *Geophys. Res. Lett.*, **23**, 1549–1552.
- Tanioka, Y. & Seno, T., 2001. Sediment effect on tsunami generation of the 1896 Sanriku tsunami earthquake, *Geophys. Res. Lett.*, **28**, 3389–3392.
- Ward, S.N., 2001. Tsunamis, in *The Encyclopedia of Physical Science and Technology*, ed Meyers, R.A. Academic, San Diego, CA.

APPENDIX A: TSUNAMI GENERATION FOR FINITE SOURCE DURATION: LINEAR POTENTIAL THEORY

The tsunami generation process was formulated based on the linear approximation by Takahashi (1942), Hammack (1973), Ward (2001) and Kervella *et al.* (2007). The basic frameworks of the formulations in these studies are common, but the final equations differ slightly. For example, Takahashi (1942) used cylindrical coordinates and assumed a symmetrical source distribution, whereas others have used Cartesian coordinates and assumed an arbitrary source distribution (Ward 2001; Kervella *et al.* 2007). Hammack (1973) and Kervella *et al.* (2007) used the Laplace transform, whereas the Fourier transform was used in other studies (Takahashi 1942). Ward (2001) assumed an instantaneous sea-bottom deformation, whereas finite duration sea-bottom deformation was assumed in other studies (Takahashi 1942; Hammack 1973). In the following, considering applicability and usability, we use Cartesian coordinates rather than the cylindrical coordinates, the Fourier transform (integral over the real axis) rather than the Laplace transform (integral over the imaginary axis) and a finite source duration rather than instantaneous sea-bottom deformation to formulate the tsunami generation process.

Assuming incompressible and irrotational flow, the velocity is represented in terms of the velocity potential ϕ as $\mathbf{u} = \nabla\phi$. The velocity potential satisfies the Laplace equation:

$$\nabla^2\phi = 0. \quad (\text{A1})$$

Based on the linear approximation, the dynamic boundary condition at the sea surface is given by

$$\left[\frac{\partial\phi}{\partial t} + 2\mu\phi \right]_{z=0} = -g\eta(x, y, t) \quad \text{for } z = 0, \quad (\text{A2})$$

where μ is the artificial damping factor and will be taken as zero in the calculation. The kinematic boundary condition at the sea surface is given by

$$\frac{\partial\eta}{\partial t} = w \quad \text{for } z = 0. \quad (\text{A3})$$

From eqs (A2) and (A3), we obtain the boundary condition of ϕ at the surface as

$$\frac{\partial^2\phi}{\partial t^2} + 2\mu\frac{\partial\phi}{\partial t} + g\frac{\partial\phi}{\partial z} = 0 \quad \text{for } z = 0. \quad (\text{A4})$$

The boundary condition at the bottom is given

$$w(x, y, z = -H) = d(x, y)\chi(t). \quad (\text{A5})$$

We obtain the velocity potential that satisfies (A1), (A4) and (A5) as

$$\begin{aligned} \phi(x, y, z, t) &= \frac{1}{2\pi} \int_{-\infty}^{\infty} d\omega \int_{-\infty}^{\infty} d\tau \exp[-i\omega(t - \tau)] \chi(\tau) \frac{1}{(2\pi)^2} \\ &\times \int_{-\infty}^{\infty} \int_{-\infty}^{\infty} dk_x dk_y \exp(ik_x x + ik_y y) \frac{1}{k} W(\omega, k, z) \hat{d}(k_x, k_y), \end{aligned} \quad (\text{A6})$$

where the function W is

$$W(\omega, k, z) = \frac{(\omega^2 + 2\mu\omega i) \sinh kz + gk \cosh kz}{(\omega^2 + 2\mu\omega i) \cosh kH - gk \sinh kH} \quad (\text{A7})$$

and $\hat{d}(k_x, k_y)$ is the 2-D spatial Fourier transform defined in eq. (10). We consider the complex ω -plane in the integration with respect to ω in eq. (A6) with eq. (A7), as follows:

$$\begin{aligned} \int_{-\infty}^{\infty} d\omega \exp[-i\omega(t - \tau)] \frac{i\omega - 2\mu}{(\omega^2 + 2\mu\omega i) \cosh kH - gk \sinh kH} \\ = \frac{2\pi}{\gamma \cosh kH} \gamma \cos[\gamma(t - \tau)] H_{\text{step}}(t - \tau), \quad \mu \rightarrow 0, \end{aligned} \quad (\text{A8})$$

where $H_{\text{step}}(t - \tau)$ is the step function.

Substituting eq. (A6) and (A8) into (A2), we obtain the sea-surface fluctuation as

$$\begin{aligned} \eta(x, y, t) &= -\frac{1}{g} \left[\frac{\partial\phi}{\partial t} + 2\mu\phi \right]_{z=0} \\ &= \frac{1}{(2\pi)^2} \int_{-\infty}^{\infty} \int_{-\infty}^{\infty} dk_x dk_y \exp[ik_x x + ik_y y] \\ &\times \int_{-\infty}^t d\tau \chi(\tau) \cos \gamma(t - \tau) \frac{1}{\cosh kH} \hat{f}(k_x, k_y). \end{aligned} \quad (\text{A9})$$

This is the same as eq. (8).

APPENDIX B: DERIVATION OF THE IMPULSE RESPONSE OF THE SEA SURFACE

We consider the sea surface fluctuation when the sea-bottom uplift is given by $\bar{d}(x, y) = \delta(x)\delta(y)$ and the deformation occurs instantaneously, $T = 0$, or the impulse response of the sea-surface

$G(\mathbf{x}, t)$ with respect to a point source of vertical velocity at the bottom. Note that we use $\bar{d}(x, y)$ instead of $d(x, y)$, because the dimension is different. Here, $d(x, y)$ has a dimension of length L , and $\bar{d}(x, y)$ has a dimension of L^{-2} . Considering that the 2-D Fourier transform of $\bar{d}(x, y) = \delta(x)\delta(y)$ is 1, the response of the point source with finite source duration T is given by

$$G(\mathbf{x}, t) = \frac{1}{(2\pi)^2} \int_{-\infty}^{\infty} \int_{-\infty}^{\infty} d\mathbf{k} \exp(i\mathbf{k} \cdot \mathbf{x}) \frac{\sin \gamma t - \sin[\gamma(t - T)]}{\gamma T} \times \frac{1}{\cosh kH} H_{\text{step}}(t). \quad (\text{B1})$$

Assuming that T approaches zero and considering the symmetry of the source, we obtain

$$G(\mathbf{x}, t) = \frac{1}{(2\pi)^2} \int_{-\infty}^{\infty} \int_{-\infty}^{\infty} d\mathbf{k} \exp(i\mathbf{k} \cdot \mathbf{x}) \cos \gamma t \frac{1}{\cosh kH} H_{\text{step}}(t) = \frac{1}{2\pi} \int_0^{\infty} dk J_0(kr) k \cos \gamma t \frac{1}{\cosh kH} H_{\text{step}}(t). \quad (\text{B2})$$

where $r = \sqrt{x^2 + y^2}$. Eq. (B2) is the impulse response of the sea-surface with respect to the point impulse vertical velocity at the bottom. When we consider the sea-surface distribution at the time of the deformation, $t = 0$, we obtain

$$G(r, 0) = \frac{1}{2\pi} \int_0^{\infty} dk J_0(kr) k \frac{1}{\cosh kH}. \quad (\text{B3})$$

Eq. (B3) is the same as eq. (15) and eq. (39) in Kajiura (1963).